

See discussions, stats, and author profiles for this publication at: <https://www.researchgate.net/publication/230688726>

Mechanism of H₂O₂ Decomposition on Transition Metal Oxide Surfaces

ARTICLE in THE JOURNAL OF PHYSICAL CHEMISTRY C · APRIL 2012

Impact Factor: 4.77 · DOI: 10.1021/jp300255h

CITATIONS

39

READS

93

4 AUTHORS:



[Cláudio M. Lousada](#)

KTH Royal Institute of Technology

15 PUBLICATIONS 172 CITATIONS

[SEE PROFILE](#)



[Adam Johannes Johansson](#)

Swedish Nuclear Fuel and Waste Management...

26 PUBLICATIONS 260 CITATIONS

[SEE PROFILE](#)



[Tore Brinck](#)

KTH Royal Institute of Technology

130 PUBLICATIONS 4,178 CITATIONS

[SEE PROFILE](#)



[Mats Jonsson](#)

KTH Royal Institute of Technology

153 PUBLICATIONS 2,446 CITATIONS

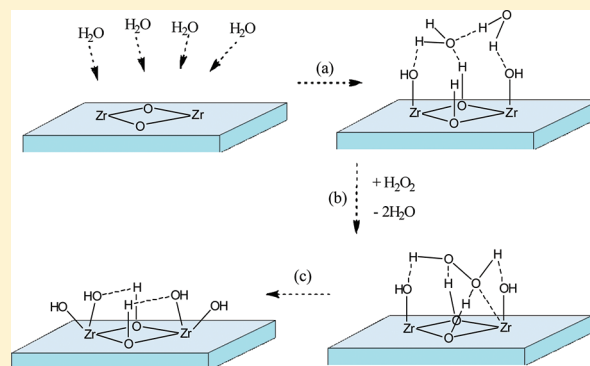
[SEE PROFILE](#)

Mechanism of H₂O₂ Decomposition on Transition Metal Oxide Surfaces

Cláudio M. Lousada,* Adam Johannes Johansson, Tore Brinck, and Mats Jonsson

Applied Physical Chemistry, School of Chemical Science and Engineering, KTH Royal Institute of Technology, SE-100 44 Stockholm, Sweden

ABSTRACT: We performed an experimental and density functional theory (DFT) investigation of the reactions of H₂O₂ with ZrO₂, TiO₂, and Y₂O₃. In the experimental study we determined the reaction rate constants, the Arrhenius activation energies, and the activation enthalpies for the processes of adsorption and decomposition of H₂O₂ on the surfaces of nano- and micrometer-sized particles of the oxides. The experimentally obtained enthalpies of activation for the decomposition of H₂O₂ catalyzed by these materials are 30 ± 1 kJ·mol⁻¹ for ZrO₂, 34 ± 1 kJ·mol⁻¹ for TiO₂, and 44 ± 5 kJ·mol⁻¹ for Y₂O₃. In the DFT study, cluster models of the metal oxides were used to investigate the mechanisms involved in the surface process governing the decomposition of H₂O₂. We compared the performance of the B3LYP and M06 functionals for describing the adsorption energies of H₂O₂ and HO• onto the oxide surfaces as well as the energy barriers for the decomposition of H₂O₂. The DFT models implemented can describe the experimental reaction barriers with good accuracy, and we found that the decomposition of H₂O₂ follows a similar mechanism for all the materials studied. The average absolute deviation from the experimental barriers obtained with the B3LYP functional is 6 kJ·mol⁻¹, while with the M06 functional it is 3 kJ·mol⁻¹. The differences in the affinity of the different surfaces for the primary product of H₂O₂ decomposition, the HO radical, were also addressed both experimentally and with DFT. With the experiments we found a trend in the affinity of HO• toward the surfaces of the oxides, depending on the type of oxide. This trend is successfully reproduced with the DFT calculations. We found that the adsorption energy of HO• varies inversely with the ionization energy of the metal cation present in the oxide.



1. INTRODUCTION

Reactions of H₂O₂ with metal and metal oxide surfaces have been studied to some extent^{1–7} mainly due to their importance in areas ranging from catalysis to geo- and environmental chemistry and nuclear technology. Due to the complexity of the systems involved, which is dominated by the heterogeneity caused by the introduction of a solid phase, several mechanistic details remain to be understood. Furthermore, effects such as solution pH, type of oxide, temperature, and oxide particle size have profound effects on the kinetics and energetics of this type of reactions.^{8–10} The reactivity of H₂O₂—an aqueous radiolysis product—toward metal and metal oxide surfaces is important in the context of nuclear technology.¹¹ The knowledge of the mechanistic details that govern this type of reactions is of the utmost importance for allowing a rigorous assessment of the chemistry of nuclear technological systems which is determinant for sensitive issues such as the reliability, stability, and safety of an operating nuclear power plant or of a repository for spent nuclear fuel.^{12,13} In spite of their importance in a variety of contexts, radiation-induced processes at solid–liquid interfaces are often poorly understood. To better understand these processes, the mechanisms and kinetics of reactions between radiolysis products in solution and the solid surfaces must be known.¹⁴

Besides being able to react through a redox path,¹⁵ H₂O₂ also reacts via catalytic decomposition.^{16,17} The latter type of reaction is typical of systems where the metal present in the oxide cannot undergo further oxidation. Nevertheless, the presence of catalytic decomposition of H₂O₂ in systems where the metal atoms have the possibility to undergo oxidation has been reported.¹⁸ Since H₂O₂ can act both as an oxidant and as a reductant, reduction of Ti⁴⁺ to Ti³⁺ by reaction of H₂O₂ with TiO₂ has also been proposed based on experimental studies.¹⁹ The initial step of the catalytic decomposition of H₂O₂ on metal oxide surfaces has been proposed to be the homolytic cleavage of the O–O bond in H₂O₂ to form two HO radicals.^{19,20} We previously reported a study in which we followed the dynamics of formation of HO radicals during the course of H₂O₂ decomposition on the surface of ZrO₂. Our findings show that the HO radical is a primary product of this type of reaction.²¹ The further reactions of the HO radicals formed in this process are still a matter that is not completely understood. It has been suggested that these radicals can react further with H₂O₂ to form HO₂• and O₂•.^{7,22,23} In previous

Received: January 9, 2012

Revised: March 27, 2012

Published: April 18, 2012

studies of this type of reaction, EPR/ESR measurements revealed the presence of HO_2^\cdot , $\text{O}_2^{\cdot-}$, and peroxy radical species on the surface of different oxides. These normally short-lived and reactive species had become long-lived due to the stabilization imparted by their adsorption onto the oxide surface.^{20,24} It was also demonstrated that the possible existence of such chemical species is a factor that depends on the solution pH. Kinetic studies on these systems have shown that for the catalytic decomposition of H_2O_2 on different metal oxide surfaces similar activation energies are involved, while the pre-exponential factors differ widely. Consequently, the rate constants differ substantially depending on the type of oxide.²⁵ This indicates that different surface processes might be involved in the reactions of H_2O_2 with the different metal oxides.

In this paper, we report a combined theoretical and experimental effort aimed at providing an understanding of the mechanisms and surface processes involved in the reactions of H_2O_2 with different metal oxides. We performed a comprehensive experimental investigation of the reactions between H_2O_2 and ZrO_2 , TiO_2 and Y_2O_3 . We studied the kinetics of such reactions, and some mechanistic aspects were addressed. The affinity of HO radicals for the different metal oxides was also studied. Density functional theory (DFT) calculations were used to study the reactions of the different oxide surfaces with H_2O_2 and HO^\cdot . The potential for using molecular cluster models to describe these systems was explored using the DFT functionals B3LYP (refs 26–29) and M06 (ref 30).

The surface processes studied in this work are represented in Figure 1. The adsorption of H_2O onto metal oxide surfaces can

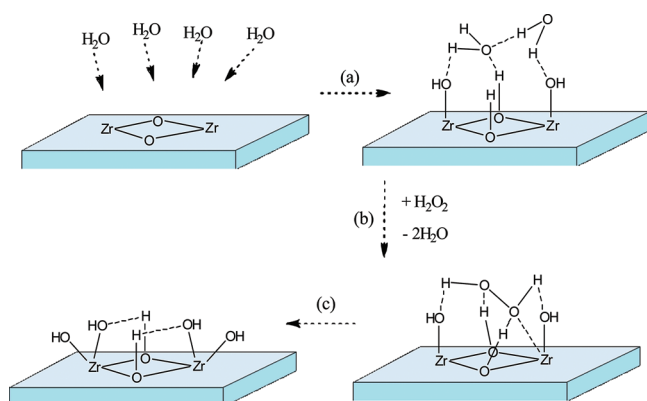


Figure 1. Surface processes studied in this work: (a) adsorption of H_2O ; (b) reaction with H_2O_2 —initial adsorption of H_2O_2 with desorption of H_2O ; and (c) formation of products of the decomposition of H_2O_2 and their adsorption to the surface.

occur via two pathways which are molecular adsorption or dissociative adsorption.³¹ It has been reported that the mode of adsorption of the first layer of water onto a metal oxide surface is in general dissociative.³² However, for certain defective metal oxide surfaces, the cleavage of water occurs spontaneously only on specific surface defects.^{32–34} The first reaction step investigated in this work by DFT was the adsorption of H_2O_2 onto the surfaces of the clusters in which H_2O had been previously dissociatively adsorbed. The energies of H_2O adsorption obtained in an undergoing work where we study the performance of similar cluster models to describe a diversity of surface processes³⁵ are compared with the available data in

the literature. These values are used as benchmarks for the performance of our cluster models. A comparison between our experimentally obtained activation enthalpies for the decomposition of H_2O_2 on the surface of the different metal oxides and the values calculated with DFT allowed us to conclude that we can, to a good extent, describe the complex chemistry of the surface reactions involved, by using small clusters comprised of $(\text{M}_x\text{O}_y)_2$ where M is the metal atom. This indicates that on the real particle surfaces, due to the dominance of surface defects, localized properties of the surface are decisive in determining the mechanism of the reaction and its kinetics and energetics.

2. EXPERIMENTAL AND COMPUTATIONAL METHODS

2.1. Instrumentation. Specific surface areas of the powders were determined using the BET method of isothermal adsorption and desorption of a gaseous mixture consisting of 30% N_2 and 70% He on a Micrometrics Flowsorb II 2300 instrument. γ -Irradiation was performed using an MDS Nordion 1000 Elite Cs-137 γ -source with a dose rate of $0.15 \text{ Gy}\cdot\text{s}^{-1}$. This value was determined by Fricke dosimetry.³⁶ X-ray powder diffractograms (XRDs) were obtained at 293.15 K, using Cu K_α radiation, on a PANalytical X'pert instrument. For all samples, the default setup with the X'Celerator was used. The data were collected over the range $10^\circ \leq 2\theta \leq 100^\circ$, with a step size of 0.033° (2θ). Data evaluation was done using The High Score Plus software package, and the PDF-2 database was used for matching the experimentally obtained diffractograms. The reactions were performed under an inert atmosphere with a constant flux of N_2 gas (AGA Gas AB) with a flow rate of $0.21 \text{ L}\cdot\text{min}^{-1}$ that was also used for stirring the solutions. The temperature was kept constant throughout the experiments by using a Huber CC1 or a Lauda E100 thermostat, calibrated against a Thermo 1 Thermometer coupled to a submersible K-type (NiCrNi) temperature probe, with a precision of $\pm 0.1 \text{ K}$. For the γ -irradiations, the samples were purged with N_2O with a flow rate of $0.7 \text{ L}\cdot\text{min}^{-1}$. UV/vis spectra were collected using a WPA Biowave II UV/vis spectrophotometer.

2.2. Reagents and Experiments. All the solutions used in this study were prepared using water from a Millipore Milli-Q system.

ZrO_2 (CAS[1314-23-4], Aldrich 99%), TiO_2 (CAS[13463-67-7], Alfa Aesar, 99.9%), and Y_2O_3 (CAS[1314-36-9], Alfa Aesar, 99.9%) were used without further purification. A Rietveld refinement using ICSD-26488 as a starting model was performed yielding the following cell parameters for ZrO_2 : (a) $5.1458(2) \text{ \AA}$, (b) $5.2083(3) \text{ \AA}$, (c) $5.3124(3) \text{ \AA}$. These values are in good agreement with the cell parameters attributed to the monoclinic phase.³⁷ For TiO_2 , the Rietveld refinement yielded a composition of 88.5% anatase and 11.5% rutile. The obtained cell parameters for TiO_2 are: ($a = b$) $3.7856(2) \text{ \AA}$, (c) $9.5058(5) \text{ \AA}$ for the anatase phase, and ($a = b$) $4.5914(8) \text{ \AA}$, (c) $2.9539(10) \text{ \AA}$ for the rutile phase.³⁸ The obtained cell parameters for Y_2O_3 are: (a) $10.60398(9) \text{ \AA}$, attributed to the bixbyite-type structure.³⁹ The specific surface areas of the powders were found to be $5.0 \pm 0.2 \text{ m}^2\cdot\text{g}^{-1}$ for ZrO_2 , $38.9 \pm 0.2 \text{ m}^2\cdot\text{g}^{-1}$ for TiO_2 , and $4.48 \pm 0.03 \text{ m}^2\cdot\text{g}^{-1}$ for Y_2O_3 . These values are the average of three measurements, each consisting of a sorption and a desorption isotherm whose values were also averaged. The particle suspensions where the reactions with H_2O_2 took place consisted of TiO_2 ($0.146\text{--}0.341 \text{ g}$) or Y_2O_3 ($1.269\text{--}2.961 \text{ g}$) in 50 mL of H_2O_2 ($0.5\text{--}6 \text{ mM}$) solution. The H_2O_2 solutions were prepared from a 30% standard solution (Merck). After extraction of the sample from

the reaction vessel, the sample was filtered through a Gema Medical 0.45 μm –25 mm Cellulose Acetate syringe filter. Subsequently, a sample volume of 0.2 mL was used for the measurement of the H_2O_2 concentration. The concentration of H_2O_2 was determined using the Ghormley triiodide method. In this method, I^- is oxidized to I_3^- by H_2O_2 .^{40,41} The absorbance of the product I_3^- is measured spectrophotometrically at the wavelength of 350 nm. A calibration curve where the absorbance of I_3^- was plotted as a function of the concentration of H_2O_2 was obtained in the range 0.02–0.8 mM resulting in a linear correlation between absorbance and concentration. A mechanistic study of the decomposition of H_2O_2 on the surface of the metal oxides was carried out and involved verifying the presence and quantifying the rate of production of HO^\bullet as intermediate product in H_2O_2 decomposition on TiO_2 and Y_2O_3 . This was done by means of the reaction between tris(hydroxymethyl)aminomethane (Tris) (CAS[77-86-1], BDH Chemicals, 99%) and the HO^\bullet radicals to produce formaldehyde. The formaldehyde produced was then quantified spectrophotometrically at 368 nm, by using a modified version of the Hantzsch reaction. We reported this method to detect the HO^\bullet radicals in a previous work,²¹ and the same procedure was followed in this study. The reaction media for HO^\bullet detection during decomposition of H_2O_2 consisted of TiO_2 (0.197 g) or Y_2O_3 (1.678 g) in 50 mL of solution H_2O_2 (5 mM) with Tris (20 mM) at a pH of 7.5. The pH was adjusted with HCl. The study of the scavenging capacities of the oxides toward HO^\bullet consisted initially of γ -irradiating samples of the oxides in the presence of Tris. The reaction media used was ZrO_2 (1.5 g) or TiO_2 (0.197 g) or Y_2O_3 (1.678 g) in 50 mL of Tris (20 mM) solution at pH 7.5. The pH was adjusted with HCl. The detection of the amount of HO^\bullet radicals scavenged by Tris followed the same procedure as described above.

2.3. Computational Details. DFT calculations were performed using the Molecular Cluster Model (MCM)⁴² approach and the software package Jaguar 7.7.⁴³ Cluster geometries were optimized using the hybrid functional B3LYP (refs 26–29) with the LACVP+* basis set. B3LYP can provide accurate molecular geometries even when hydrogen bonds are present.⁴⁴ The basis set LACVP+* is a combination of the split valence basis set 6-31+G(d) and the Los Alamos effective core potential for the transition metals Zr, Ti, and Y. Single-point evaluations of the energies were performed at the B3LYP/LACVP++** and M06 (ref 30)/LACVP++** levels of theory. The basis set LACVP++** is triple- ζ in the valence space and is supplemented with polarization and diffuse functions on all atoms. Tight SCF convergence criteria were used for all calculations. Transition states were located using the quadratic synchronous transit (QST) method implemented in Jaguar 7.7. To characterize the stationary points and make zero-point energy corrections, a frequency analysis was done for all stationary points. All transition states were found to have one imaginary frequency.

The adsorption energies reported herein were calculated as

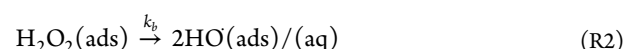
$$\Delta E_{\text{ads}} = E_{\text{adsorbate/cluster}} - (E_{\text{adsorbate}} + E_{\text{cluster}}) \quad (1)$$

where $E_{\text{adsorbate/cluster}}$, $E_{\text{adsorbate}}$, and E_{cluster} represent the optimized electronic energies in the gas phase for the adsorbate binding to the cluster, free adsorbate, and bare cluster, respectively. This means that the more negative the electronic adsorption energy, the stronger is the adsorption.

Corrections to obtain the thermodynamic potential enthalpy (H) were calculated from a Hessian matrix of harmonic force constants using the partition functions of an ideal/non-interacting gas at $T = 298.15$ K and $P = 1$ atm. The vibrational frequencies obtained from the Hessian matrix were also used to verify the first-order saddle point nature of the transition states.

3. RESULTS AND DISCUSSION

3.1. Experimental Results. **3.1.1. Kinetics of Decomposition of H_2O_2 on ZrO_2 , TiO_2 , and Y_2O_3 .** The reaction of H_2O_2 with a solid catalyst which in this case is a metal oxide of the type M_xO_y consists of a series of steps characteristic of cycling surface-catalyzed reactions. The first step is the diffusion and adsorption of H_2O_2 to the surface followed by its cleavage to form HO^\bullet . One can write these two processes as



where reaction R1 represents the adsorption of H_2O_2 onto the oxide surface and R2 represents the cleavage of H_2O_2 catalyzed by the oxide surface to form HO^\bullet radicals. k_{a} is the rate constant of adsorption of H_2O_2 ; $k_{\text{a}'}$ is the rate constant of desorption; and k_{b} is the rate constant for the cleavage of H_2O_2 on the surface of the metal oxide. When the surface is saturated with adsorbate, the rate of disappearance of H_2O_2 from solution will be governed by k_{b} of reaction R2. Hence, a quasi-equilibrium state is reached.⁴⁵

It has been reported that the catalytic decomposition of H_2O_2 follows first-order kinetics.^{46–48} However, the observed reaction order is strongly dependent on the solid-surface-area-to-solution-volume-ratio (S_{A}/V) and other experimental conditions.²¹ When the available surface area of the catalyst is in excess, first-order kinetics are observed. Zeroth-order kinetics are observed when the available surface area is too small. In this work, using the same S_{A}/V as we used to obtain first-order kinetics in the case of ZrO_2 ,²¹ it was verified that the reactions of H_2O_2 with TiO_2 and Y_2O_3 deviated from first-order kinetic behavior, and two different trends can be observed in the plots of Figure 2 where $[\text{H}_2\text{O}_2]_t$ is the concentration of H_2O_2 at time t and $[\text{H}_2\text{O}_2]_0$ is the concentration of H_2O_2 at $t = 0$. In both cases, after a fast initial consumption of H_2O_2 , the reaction is slowed down significantly. To extract the rate constants, we considered the two visible trends for each reaction in Figure 2

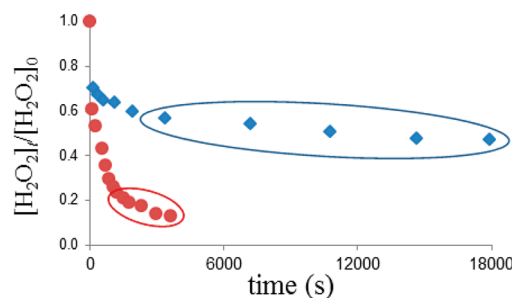


Figure 2. Normalized concentration of H_2O_2 as a function of reaction time in the reaction of H_2O_2 with TiO_2 (blue diamond) and Y_2O_3 (red circle) at $T = 298.15$ K with $[\text{H}_2\text{O}_2]_0 = 0.5$ mM. The highlighted areas denote the regions where the kinetics start to be controlled by the decomposition of H_2O_2 after the initial adsorption process.

to be the result of two different processes governing the kinetics. The nature of the two different kinetic trends of this reaction were investigated by performing the reaction in the presence of Tris buffer and tracking the formation of CH_2O with reaction time. Verifying if HO^\bullet is formed during the stage of initial fast disappearance of H_2O_2 from solution is essential to make valid statements regarding the surface process involved. The process can be either molecular adsorption of H_2O_2 onto the surface or decomposition of H_2O_2 or a mixed adsorption/decomposition phenomenon. The reaction of H_2O_2 (5 mM) with TiO_2 (0.537 g) was performed in a volume of 50 mL of Tris (200 mM) solution at pH 7.5. The pH was adjusted with HCl.

It can be seen in Figure 3 that the initial disappearance of H_2O_2 from solution is not accompanied by the formation of a

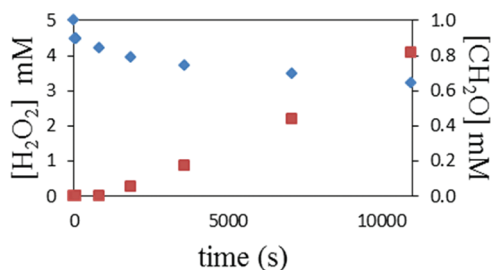


Figure 3. Evolution in the concentrations of H_2O_2 (blue diamond) and CH_2O (red square) during the reaction of H_2O_2 with a particle suspension of TiO_2 at $T = 298.15$ K.

detectable amount of HO radicals. From the calibration experiments, a consumption of the equivalent amount of H_2O_2 (0.5 mM) that disappeared from solution in the initial process would produce ~ 0.18 mM CH_2O . From Figure 3, we can see that this is not the case. Hence, we can conclude that the initial fast disappearance of H_2O_2 can be attributed to molecular adsorption of this species onto the surface of the TiO_2 . We can attribute the two different kinetic trends represented in Figure 2 and Figure 3 to the following processes: an initial adsorption step followed by a second process that consists of the cleavage of H_2O_2 on the surface of the oxide. By extracting the rate constants from these plots, taking into account the fact that the two processes, adsorption and decomposition of H_2O_2 , occur on different time scales, it is possible to obtain the kinetics of decomposition of H_2O_2 with minimal errors associated.

The kinetic experiments were performed using H_2O_2 (0.5 mM) with TiO_2 (0.197 g) or Y_2O_3 (1.67 g) in 50 mL of H_2O . The zeroth-order rate constants (k_0) obtained at $T = 298.15$ K, with a $(S_A/V) = 1.4 \times 10^5 \text{ m}^{-1}$ for TiO_2 and $1.5 \times 10^5 \text{ m}^{-1}$ for Y_2O_3 are $k_0 = (5.9 \pm 0.6) \times 10^{-6} \text{ M}\cdot\text{s}^{-1}$ for the decomposition of H_2O_2 on TiO_2 and $k_0 = (4.5 \pm 0.4) \times 10^{-5} \text{ M}\cdot\text{s}^{-1}$ for the decomposition of H_2O_2 on Y_2O_3 . The rate constants for adsorption under the same conditions were extracted from the initial parts of the plots. The obtained first-order rate constants (k_1) for this process are $k_1 = 3 \times 10^{-3} \text{ s}^{-1}$ for adsorption of H_2O_2 on TiO_2 and $k_1 = 6 \times 10^{-3} \text{ s}^{-1}$ for adsorption of H_2O_2 on Y_2O_3 .

The variation of the rate constant with temperature generally follows the Arrhenius equation

$$k = Ae^{-E_a/RT} \quad (2)$$

where E_a is the Arrhenius activation energy for the reaction; A is the pre-exponential or the frequency factor; R is the gas constant; and T is the absolute temperature. The respective reaction enthalpies of activation were obtained by means of a linearization of the Eyring equation

$$\ln\left(\frac{k}{T}\right) = -\frac{\Delta H^{\ddagger}}{RT} + \frac{\Delta S^{\ddagger}}{R} + \ln\left(\frac{k_B}{h}\right) \quad (3)$$

where k is the reaction rate constant; T is the absolute temperature; ΔH^{\ddagger} is the enthalpy of activation; R is the gas constant; k_B is the Boltzmann constant; h is the Planck constant; and ΔS^{\ddagger} is the entropy of activation. To determine the Arrhenius activation energies and the activation enthalpies for the reactions of decomposition of H_2O_2 on TiO_2 and Y_2O_3 , we obtained the zeroth-order rate constants as a function of temperature in the temperature intervals $T = [298.15\text{--}348.15]$ K for TiO_2 and $T = [293.15\text{--}308.15]$ K for Y_2O_3 . The respective Arrhenius plots are represented in Figure 4. The

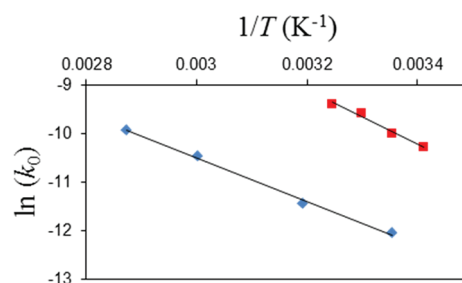


Figure 4. Arrhenius plots for the reaction of decomposition of H_2O_2 on TiO_2 (blue diamond) and Y_2O_3 (red square).

resulting activation energies for decomposition of H_2O_2 on TiO_2 and Y_2O_3 are $37 \pm 1 \text{ kJ}\cdot\text{mol}^{-1}$ and $47 \pm 5 \text{ kJ}\cdot\text{mol}^{-1}$, respectively. The pre-exponential factors are $18 \pm 2 \text{ M}\cdot\text{s}^{-1}$ for TiO_2 and $6228 \pm 6 \text{ M}\cdot\text{s}^{-1}$ for Y_2O_3 . The activation enthalpies ΔH^{\ddagger} for H_2O_2 decomposition are $34 \pm 1 \text{ kJ}\cdot\text{mol}^{-1}$ for TiO_2 and $44 \pm 5 \text{ kJ}\cdot\text{mol}^{-1}$ for Y_2O_3 .

The activation energies of adsorption $E_{a,\text{ads}}$ were calculated from plots of the logarithm of the first-order rate constants as a function of the inverse of the temperature. The activation enthalpies of adsorption $\Delta H_{\text{ads}}^{\ddagger}$ were determined by using the same first-order rate constants. The first-order rate constants for adsorption were extracted from the initial parts of the plots of $\ln([\text{H}_2\text{O}_2]_t/[\text{H}_2\text{O}_2]_0)$ as a function of reaction time. The resulting activation energies for adsorption are $E_{a,\text{ads}} = 23 \pm 1 \text{ kJ}\cdot\text{mol}^{-1}$ for adsorption of H_2O_2 on TiO_2 and $E_{a,\text{ads}} = 32 \pm 3 \text{ kJ}\cdot\text{mol}^{-1}$ for adsorption of H_2O_2 on Y_2O_3 . The frequency factors are $A = 21 \pm 2 \text{ s}^{-1}$ for the adsorption on TiO_2 and $A = 2625 \pm 3 \text{ s}^{-1}$ for the adsorption on Y_2O_3 . The activation enthalpies of adsorption are $\Delta H_{\text{ads}}^{\ddagger} = 21 \pm 2 \text{ kJ}\cdot\text{mol}^{-1}$ for adsorption of H_2O_2 onto TiO_2 and $\Delta H_{\text{ads}}^{\ddagger} = 29 \pm 3 \text{ kJ}\cdot\text{mol}^{-1}$ for adsorption of H_2O_2 onto Y_2O_3 .

The second-order rate constants for the process of adsorption were determined by studying the variation of the pseudo first-order rate constants as a function of solid-surface-area-to-solution-volume-ratio. The rate expression for the adsorption process is given by

$$-\frac{d[\text{H}_2\text{O}_2]}{dt} = k_2 \left(\frac{S_{A,\text{MxOy}}}{V} \right) [\text{H}_2\text{O}_2] \quad (4)$$

where $S_{A_{\text{MeOx}}}$ denotes the surface area of the metal oxide powder; V is the volume of the solution where the reaction takes place; and k_2 is the second-order rate constant. The second-order rate constants for adsorption of H_2O_2 onto the surfaces of TiO_2 and Y_2O_3 were obtained from experiments in which the first-order rate constants were determined for different oxide S_A values. The resulting data are represented in Figure 5. The second-order rate constants extracted from the

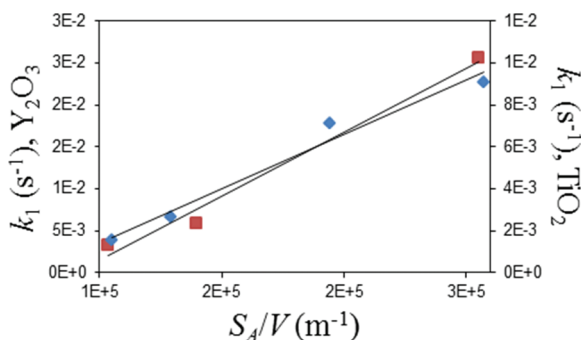


Figure 5. First-order rate constants as a function of solid-surface-area-to-solution-volume-ratio (S_A/V) for the adsorption of H_2O_2 onto Y_2O_3 (red square) and TiO_2 (blue diamond) at $T = 298.15$ K.

plots of Figure 5 obtained at $T = 298.15$ K are $k_2 = (5.2 \pm 0.6) \times 10^{-8} \text{ m}\cdot\text{s}^{-1}$ for adsorption of H_2O_2 onto TiO_2 and $k_2 = (1.5 \pm 0.2) \times 10^{-7} \text{ m}\cdot\text{s}^{-1}$ for adsorption of H_2O_2 onto Y_2O_3 . These values are far from the diffusion limit of systems containing particle suspensions within this size range.¹⁴ A plot of the variation of the zeroth-order rate constant for decomposition of H_2O_2 as a function of S_A/V gives the rate constant k which represents the catalytic capacity of the surface. The rate constants extracted from the plots of Figure 6, obtained at $T =$

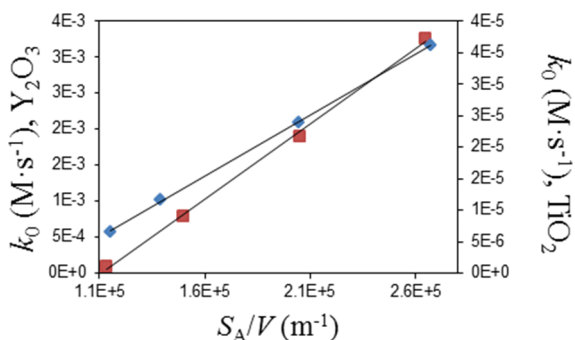


Figure 6. Zeroth-order rate constants as a function of solid-surface-area-to-solution-volume-ratio (S_A/V) for the reactions of decomposition of H_2O_2 with Y_2O_3 (red square) and TiO_2 (blue diamond) at $T = 298.15$ K.

298.15 K, are $k = (1.93 \pm 0.02) \times 10^{-13} \text{ mol}\cdot\text{m}^{-2}\cdot\text{s}^{-1}$ for reaction with TiO_2 and $k = (2.08 \pm 0.06) \times 10^{-11} \text{ mol}\cdot\text{m}^{-2}\cdot\text{s}^{-1}$ for reaction with Y_2O_3 .

In the plots of Figure 1, it can be seen that it is possible to distinguish between the adsorption and the decomposition processes because the latter process is slower than the former. This allows us to determine the amount of H_2O_2 removed from solution during the adsorption process which is directly dependent on the number of adsorption sites on the surface of the oxides that can accommodate H_2O_2 . By determining the amount of H_2O_2 removed from solution due to adsorption as a

function of the oxide surface area, we can estimate the number of adsorption sites per unit surface area of the oxide. Increasing the surface area of oxide increases the amount of H_2O_2 removed from solution by adsorption. The proportionality coefficient between these two quantities gives the number of adsorption sites available to accommodate H_2O_2 per unit surface area. The amount of H_2O_2 removed from solution as a function of TiO_2 and Y_2O_3 surface areas is represented in Figure 7. The number of adsorption sites that can

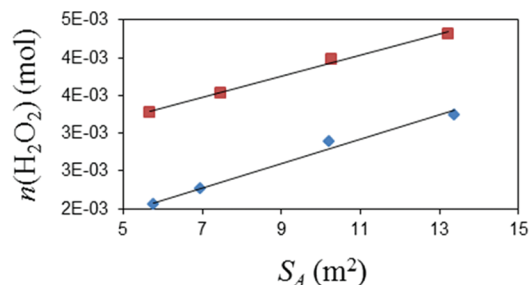


Figure 7. Variation in the amount (n) of H_2O_2 molecules removed from solution by adsorption onto TiO_2 (blue diamond) and Y_2O_3 (red square) as a function of the surface area of solid present in the reaction system.

accommodate H_2O_2 , extracted from the slopes of the plots, is $2 \times 10^{-4} \text{ mol}\cdot\text{m}^{-2}$ for TiO_2 and $1 \times 10^{-4} \text{ mol}\cdot\text{m}^{-2}$ for Y_2O_3 . These values correspond to 1.2 (adsorption sites)/ \AA^2 for TiO_2 and 0.6 (adsorption sites)/ \AA^2 for Y_2O_3 .

3.1.2. Study of the Affinity of HO^\bullet for Metal Oxide Surfaces. Water radiolysis and the products formed therein are well documented in the literature. During the process of water radiolysis induced by γ radiation, for times greater than 10^{-6} s after energy deposition, the radiation chemical yields for the solvated electrons (e_{aq}^-) and HO^\bullet are the same.⁴⁹ Upon saturation of the aqueous phase with N_2O before and during irradiation, e_{aq}^- is quantitatively converted to HO^\bullet .⁵⁰

We investigated the scavenging capabilities of the different metal oxides toward HO^\bullet present in solution. This was done by γ -irradiating aqueous powder suspensions of the different oxides in the presence of Tris. The competition for HO^\bullet between Tris and the surface of the oxides can give us a picture of the differences in the abilities of the different oxides to scavenge HO^\bullet from solution. A background plot was obtained to determine the yield of the method in a similar way as described in a previous work.²¹ To obtain the background, the reaction media consisted of a solution of Tris (20 mM) at pH 7.5 adjusted with HCl in 50 mL of H_2O , continuously purged with N_2O . The yield of the method— CH_2O formed per total amount of HO^\bullet formed—is $\approx 35\%$. In the scavenging capability experiments, ZrO_2 (1.5 g, $S_A = 7.5 \text{ m}^2$) or TiO_2 (0.197 g, $S_A = 7.5 \text{ m}^2$) or Y_2O_3 (1.678 g, $S_A = 7.5 \text{ m}^2$) were added to a solution with the same volume and composition as described above. Plots showing the amount of HO^\bullet detected as a function of irradiation time are represented in Figure 8. After irradiating the system for 1600 s, the different scavenging capacities of the different metal oxides toward HO^\bullet start to become evident. This fact can provide a qualitative measure of the affinity of HO^\bullet toward the surfaces of the oxides. The affinity of HO^\bullet toward the surfaces of the oxides is expected to control the relative kinetics for adsorption, desorption, and eventual diffusion of HO^\bullet on the surface.⁵¹ According to the plots, the HO^\bullet affinity toward the surfaces vary in the order: $\text{TiO}_2 < \text{ZrO}_2$

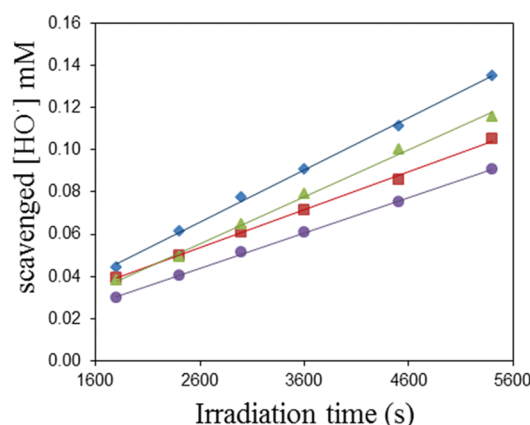


Figure 8. $[\text{HO}^\bullet]$ measured in γ -irradiated solutions with and without the presence of different metal oxides. No oxide (blue diamond); TiO_2 (green triangle); ZrO_2 (red square); and Y_2O_3 (purple circle).

$< \text{Y}_2\text{O}_3$. The amount of HO^\bullet scavenged from solution by the metal oxide depends on the (S_A/V) of the metal oxide present in the system. Consequently, the amount of HO^\bullet detected varies inversely with metal oxide (S_A/V) .

3.2. Computational Results. In this section, we discuss results of DFT calculations on the reactions of H_2O , H_2O_2 , and HO^\bullet with stoichiometric clusters of ZrO_2 , TiO_2 , and Y_2O_3 . The clusters studied are of the type $(\text{ZrO}_2)_2$, $(\text{TiO}_2)_2$, and (Y_2O_3) . The choice for using these model sizes is based on an ongoing work where we verified that the type of reactions studied here can be modeled using minimal sized clusters for describing the metal oxides (work to be published).³⁵ There are several examples in the literature where it is shown that energy

barriers for reactions catalyzed by surface sites where the metal atoms are undercoordinated can be much lower than the energy barriers for equivalent reactions catalyzed by non-defective surfaces.^{52–54} Consequently, for defective surfaces, the overall reaction rate is often determined by processes occurring at defect sites.⁵⁵ The physical-chemical properties of the defects and consequently the chemical reactivity of such surface sites are the result of the local properties of the defect and not so much dependent on the properties of the extended surface.

In our cited work,³⁵ the performance of the models used here is compared with the performance of larger clusters. The clusters used in this work can reproduce with small deviation the data obtained with clusters composed of 8 and 12 units of (M_xO_y) where M is the metal present in the oxide. The cluster performance in reproducing adsorption energies was evaluated by benchmarking the water adsorption energies against experimental and computational data found in the literature. The data can be found in Table 1. The overall performance of our models for describing water adsorption energies is good. The adsorption of water, both molecular and dissociative, can be modeled with good agreement between experimental and computational data using our minimal sized clusters to represent the metal oxides. The same clusters are used in this work to study the surface processes involved in the catalytic decomposition of H_2O_2 catalyzed by metal oxide particles. It should be noted that these particle surface topologies are dominated by defects. As H_2O adsorption is dissociative in most of the metal oxide defective surface sites,³¹ the clusters where the reaction with H_2O_2 was performed had previously been saturated with the products of H_2O adsorption. These products are HO^- and H^+ which bind to a surface metal and

Table 1. ΔE_{ads} Obtained with DFT Calculations for the Adsorption Reactions Represented in Figures 9–12 and Data Found in the Literature for Comparison^a

ZrO_2				
data	H_2O molecular adsorption	H_2O dissociative adsorption	H_2O_2 molecular adsorption	HO^\bullet adsorption
B3LYP	−80	−115	−121	−503
M06	−93	−129	−141	−514
literature - experimental	−(44) ^{b60}	−(119; 142) ^{b; 60} −(70–94) ^{b61}	—	—
literature - theoretical	−(42–100) ^{c; 62} −(57) ^{c63}	−(194–208) ^{c; 64} −(91–170) ^{c62}	—	−(498) ^{c63}
TiO_2				
data	H_2O molecular adsorption	H_2O dissociative adsorption	H_2O_2 molecular adsorption	HO^\bullet adsorption
B3LYP	−45	−146	−58	−382
M06	−52	−160	−81	−403
literature - experimental	−(48–68) ^{b65}	—	—	—
literature - theoretical	−(71–79) ^{c; 66} −(90) ^{c; 67} −(83) ^{c68}	−(22–153) ^{c; 66} −(141) ^{c67}	−(4–78) ^{c69}	—
Y_2O_3				
data	H_2O molecular adsorption	H_2O dissociative adsorption	H_2O_2 molecular adsorption	HO^\bullet adsorption
B3LYP	−70	−86	−83	−541
M06	−76	−96	−99	−550
literature - experimental	—	−(91) ^{b; 70} −(38–99) ^{b71}	—	—
literature - theoretical	—	—	—	—

^aAll values in $\text{kJ}\cdot\text{mol}^{-1}$ —per mole of adsorbate. ^bRefers to an ΔH_{ads} . ^cRefers to an ΔE_{ads} without zero-point energy corrections.

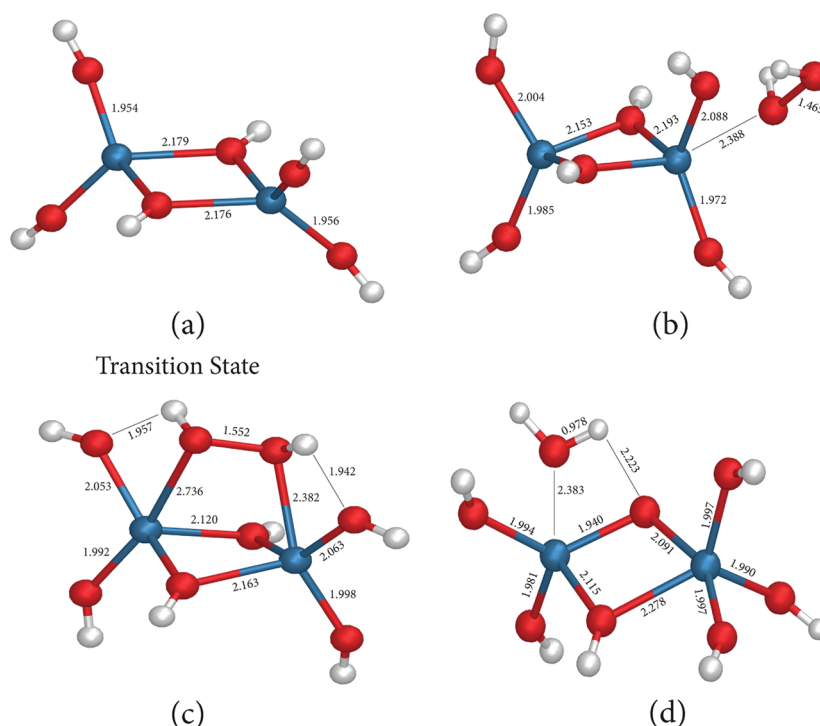


Figure 9. Optimized geometries for adsorption and further decomposition of H_2O_2 on a $(\text{ZrO}_2)_2$ cluster: (a) bare cluster, (b) chemisorption of a H_2O_2 molecule, (c) transition-state for the cleavage of the O–O bond in H_2O_2 , (d) product of the decomposition of H_2O_2 . Zr (blue); O (red); H (white).

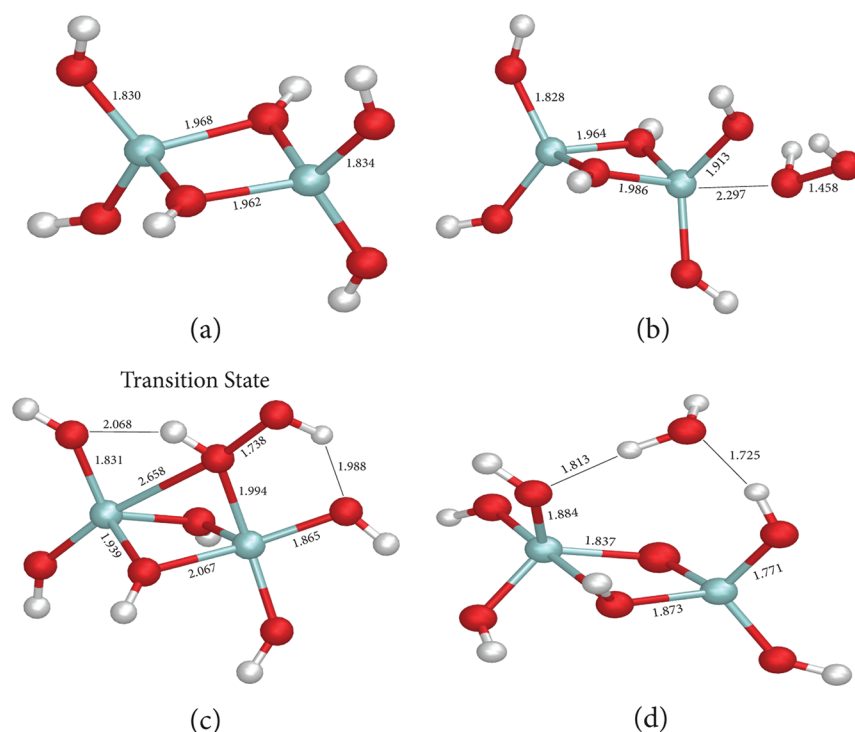


Figure 10. Optimized geometries for the study of adsorption and further decomposition of H_2O_2 in reaction with a $(\text{TiO}_2)_2$ cluster: (a) bare cluster, (b) chemisorption of a H_2O_2 molecule, (c) transition-state for the cleavage of the O–O bond in H_2O_2 , (d) product of the decomposition of H_2O_2 . Ti (cyan); O (red); H (white).

oxygen atoms, respectively. The structures of the resulting products are represented in Figures 9(a), 10(a), and 11(a).

To study the reactions of our clusters with H_2O_2 , we investigated the molecular adsorption of this species as being the first step of the reaction of decomposition of H_2O_2 on the

surface of the metal oxides. Energy minima geometries corresponding to the molecular adsorption of H_2O_2 onto the surface of the clusters were found for the three materials studied. The corresponding structures are depicted in Figures 9(b), 10(b), and 11(b). The obtained adsorption energies are

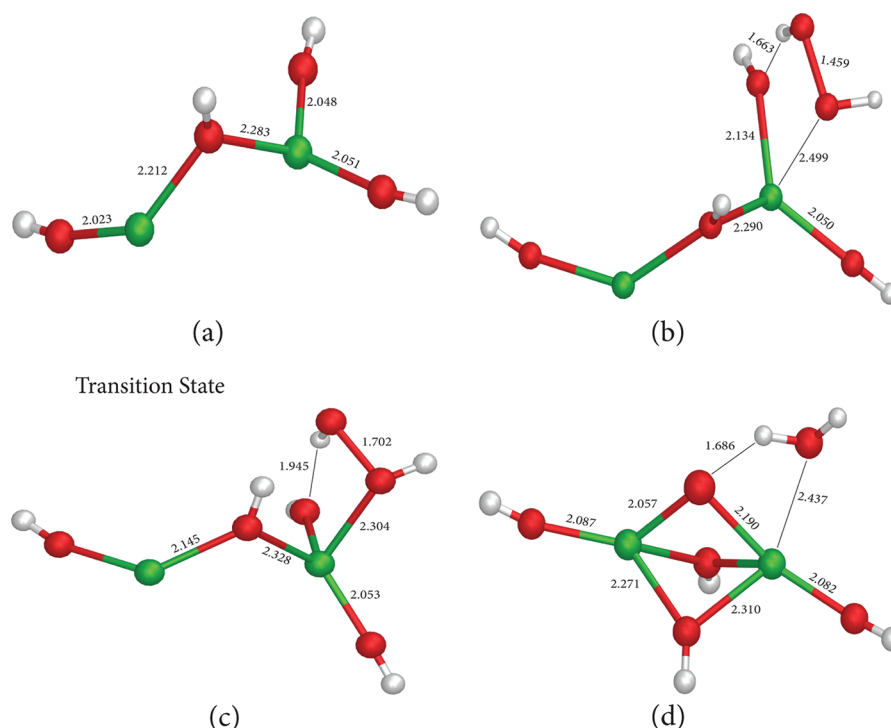


Figure 11. Optimized geometries for the study of adsorption and further decomposition of H_2O_2 in reaction with a $(Y_2O_3)_3$ cluster: (a) bare cluster, (b) chemisorption of a H_2O_2 molecule, (c) transition-state for the cleavage of the O–O bond in H_2O_2 , (d) product of the decomposition of H_2O_2 . Y (green); O (red); H (white)

given in Table 1. The molecular adsorption energies obtained for H_2O_2 lie in the range of the molecular adsorption energies reported for H_2O , the adsorption of the former being slightly more exothermic than that of H_2O . This was expected given that these two chemical species adsorb onto the cluster surfaces through a similar process which is largely mediated by hydrogen bonding. The fact that H_2O_2 adsorbs to the metal oxides stronger than H_2O is an explanation for the fact that in the kinetic experiments represented in Figure 2 it is possible to observe an adsorption process that precedes the decomposition. The existence of molecular adsorption of H_2O_2 as the first step of the reaction of its decomposition on the surfaces of the metal oxides studied can be inferred also from the experiments reported above where the consumption of H_2O_2 and the formation of HO^\bullet were tracked simultaneously and are represented in Figure 3. As already described above, the initial process responsible for the disappearance of H_2O_2 from solution is molecular adsorption according to the experimental results. The energy minima geometries corresponding to adsorption, found with the DFT calculations, agree well with this experimental evidence. Both the M06 and B3LYP functionals are able to describe these adsorption energies following a similar trend. For all the materials studied, the molecular adsorption of H_2O_2 is slightly more exothermic—up to 23 $\text{kJ}\cdot\text{mol}^{-1}$ —when computed with the M06 functional. Given the scarcity of literature data for molecular adsorption of H_2O_2 onto the materials studied, we cannot benchmark the performance of the two functionals in describing this process.

The transition state geometries for the cleavage of the O–O bond in H_2O_2 are represented in Figures 9(c), 10(c), and 11(c). The enthalpy barriers for the decomposition of H_2O_2 can be found in Table 2. The reactants for these reactions have the structures shown in Figures 9(b), 10(b), and 11(b), where H_2O_2 is molecularly adsorbed to the surface of the clusters.

Table 2. Experimental ΔH^\ddagger and DFT Obtained ΔH^\ddagger and ΔE^\ddagger for the Decomposition of H_2O_2 ^a

material	experimental	DFT ΔH^\ddagger		DFT ΔE^\ddagger	
	ΔH^\ddagger	B3LYP	M06	B3LYP	M06
ZrO ₂	30 ± 1 ^b	37	33	38	36
TiO ₂	34 ± 1	29	29	31	31
Y ₂ O ₃	44 ± 5	23	38	23	38

^aThe DFT barriers were obtained using the LACV3P++** basis set and clusters of the type $(ZrO_2)_2$, $(TiO_2)_2$, and $(Y_2O_3)_3$ represented in Figures 9, 10, and 11, respectively. Values in $\text{kJ}\cdot\text{mol}^{-1}$ in the gas phase.

^bValue recalculated from reference 21.

There is a very good agreement between the experimentally obtained enthalpy barriers and the DFT obtained ones, especially with the M06 functional. The larger discrepancy between experimental and DFT values is for the reaction barrier calculated with the B3LYP functional in the case of Y_2O_3 . In this case, the B3LYP functional underestimated the reaction barrier by 21 $\text{kJ}\cdot\text{mol}^{-1}$. The M06 functional could reproduce this barrier with better accuracy, only 6 $\text{kJ}\cdot\text{mol}^{-1}$ lower than the experimental value. This leads us to conclude that our models, in spite of their small size, are able to reproduce with good accuracy the processes responsible for the apparent reaction energy barriers that exist in the real systems. Overall, M06 performs better than B3LYP for the reaction barriers. This can be attributed to that noncovalent interactions such as hydrogen bonding play an important role in the obtained geometries of reactants and transition-states; the latter are mediated by multiple hydrogen bondings between H_2O_2 and the surface HO groups. The M06 functional performs better in describing these types of systems where noncovalent interactions are present and dispersion effects are large.^{56–58} The products of H_2O_2 decomposition are represented in

Figures 9(d), 10(d), and 11(d). The products consist of HO radicals in all the cases. This is in agreement with the experimental results shown above in Figure 3 and with the results published in a previous work by our group that point toward the existence of HO radicals as a primary product of the decomposition of H_2O_2 when catalyzed by the surface of transition metal oxides.²¹ The two HO radicals initially formed can have different fates. From the products of the reaction of H_2O_2 , it can be seen that one HO radical can adsorb to the surface by bonding with a metal atom, while the other can remove a surface H[•] initially bound to a surface oxygen atom, to form physisorbed H_2O . The formation of H_2O due to the reaction of a HO[•] with the surface of the wet clusters is in agreement with the experimental evidence that D_2O is formed upon exposure of DO saturated surfaces to DO radicals.⁵⁹ The obtained reaction enthalpies for decomposition of H_2O_2 are shown in Table 3.

Table 3. ΔH and ΔE for the Reactions of Decomposition of H_2O_2 on the Surface of $(\text{ZrO}_2)_2$, $(\text{TiO}_2)_2$, and (Y_2O_3) Clusters Obtained with the B3LYP and M06 Functionals^a

cluster	B3LYP ΔH	M06 ΔH	B3LYP ΔE	M06 ΔE
$(\text{ZrO}_2)_2$	−617	−605	−613	−608
$(\text{TiO}_2)_2$	−493	−488	−494	−485
(Y_2O_3)	−679	−681	−678	−678

^aValues in $\text{kJ}\cdot\text{mol}^{-1}$ in the gas phase.

The large exothermicity of the reaction of cleavage of the O–O bond in H_2O_2 and formation of adsorbed HO radicals can be attributed to the process of adsorption of the later species. Both B3LYP and M06 reaction enthalpies differ very little for all the metal oxides with the largest difference for the case of ZrO_2 which is $12\text{ kJ}\cdot\text{mol}^{-1}$. The reaction of two HO radicals with the metal oxide clusters was also studied and leads to the formation of stable species. The obtained geometries are represented in Figure 12.

The energies for adsorption of HO[•] onto the surfaces of $(\text{ZrO}_2)_2$, $(\text{TiO}_2)_2$, and (Y_2O_3) presented in Table 1 are of similar magnitude. The only value found in the literature for which first-principles molecular dynamics with periodic boundary conditions was used to calculate the adsorption energy of HO[•] onto the surface of ZrO_2 is in good agreement with the values obtained in this work. The adsorption energies of HO[•] vary in the order of decreasing exothermicity $\text{Y}_2\text{O}_3 > \text{ZrO}_2 > \text{TiO}_2$. This is in excellent agreement with our

experimentally obtained trends for HO[•] adsorption energies onto the surface of these materials which are visible in Figure 8. The good agreement between experimental and DFT data is also relevant to note that the ionization energies of the metal cations present in the metal oxides studied vary in the order: $\text{Y}^{3+} < \text{Zr}^{4+} < \text{Ti}^{4+}$. Clearly the HO[•] adsorption exothermicity varies inversely with the ionization energies of the metal ions present in the oxides. The higher the ionization energy of the metal cation present in the oxide, the weaker is the adsorption of HO[•] onto that metal oxide; this is because the HO[•] adsorbs onto the metal oxide by forming bonding states with the metal atom.

Overall, there is a good agreement between the data obtained with our minimal sized cluster models and the literature and experimental values. Whereas to describe a perfect surface of a conductor or semiconductor a large model is necessary to correctly account for the delocalized electronic states of the material, a smaller model can be a good descriptor to describe a defective surface like the case of our particles. This is because the electronic states of the metal oxides are not as delocalized on the surface defective sites as they are on a perfect surface. This makes the local properties of the defect, such as the type of metal atom present and its intrinsic properties, the factors that will have a larger contribution to the adsorption energies and reaction energy barriers. Furthermore, on defective surfaces, effects such as diffusion of adsorbates across the plane of the surface will be hindered when compared to the same phenomena occurring on a perfect surface.

4. CONCLUSIONS

The kinetic experiments on the decomposition of H_2O_2 together with the experiments on HO[•] detection show the existence of an adsorption step prior to decomposition. This type of process is also predicted with the DFT calculations. The decomposition of H_2O_2 follows a similar mechanism for the three metal oxides studied. The obtained transition states are largely mediated by hydrogen bonding between H_2O_2 and surface HO groups. Nevertheless, direct interaction between the oxygen atoms of H_2O_2 and the metal atoms present in the oxide was also observed in the geometries of the transition states. The formation of two HO radicals as the primary product of the decomposition of H_2O_2 is confirmed with both the DFT calculations and the experiments. One of these radicals can further abstract a H atom initially bound to a surface O and form H_2O . The other HO radical can adsorb to the surface by forming bonding states with the metal cation

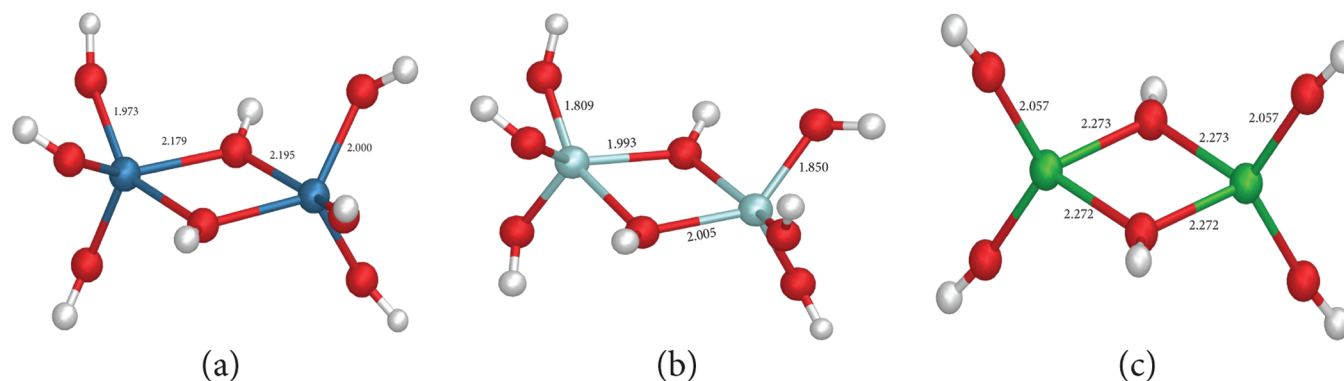


Figure 12. Optimized geometries for the adsorption of two HO radicals onto each of the clusters previously saturated with two H_2O molecules: (a) $(\text{ZrO}_2)_2$, (b) $(\text{TiO}_2)_2$, and (c) (Y_2O_3) .

present in the oxides. The experimental method used for the study of the scavenging capacities of the metal oxides toward HO^\bullet formed during γ radiolysis of H_2O gave us a qualitative measure of the affinity of HO^\bullet toward the metal oxide surfaces present in the system undergoing radiolysis. The obtained trend for adsorption energies of HO^\bullet onto the different metal oxides is inversely proportional to the variation in ionization potential of the metal cation. The trend obtained in these experiments was reproduced successfully with the DFT calculations.

The overall performance of our theoretical models, especially at the M06/LACV3P++** level, is very good. The local properties of the defects are crucial for the surface reaction of decomposition of H_2O_2 catalyzed by metal oxide particles. The extended surface effects are minimized, and these types of systems which have surfaces dominated by defects can be described by small model systems. Given the reduced coordination of the metal atoms in the clusters and since these models could describe with good accuracy the barriers for reactions catalyzed by real particles, in the real systems, catalysis by the defects where the exposed metal atoms are under-coordinated is expected to be of importance in determining the apparent reaction energy barrier. Nevertheless the type of metal atom present in a surface defect on the oxide and its stoichiometry are the most important factors that will determine the height of the barrier for the reaction catalyzed by the surface defect.

AUTHOR INFORMATION

Corresponding Author

*Phone: (46) 8 790 87 89. Fax: (46) 8 790 87 72. E-mail: cmlp@kth.se.

Notes

The authors declare no competing financial interest.

ACKNOWLEDGMENTS

The research described here was financially supported by the Swedish Centre for Nuclear Technology—SKC. Tore Brinck acknowledge financial support from the SSF program “Micro-structure, Corrosion and Friction Control”.

REFERENCES

- (1) Soleymani, M.; Moheb, A.; Babakhani, D. *Chem. Eng. Technol.* **2011**, *34*, 49.
- (2) Rasti, N.; Toyserkani, E.; Ismail, F. *Mater. Lett.* **2011**, *65*, 951.
- (3) Pehrman, R.; Amme, M.; Roth, O.; Ekeröth, E.; Jonsson, M. *J. Nucl. Mater.* **2010**, *397*, 128.
- (4) Park, J. N.; Shon, J. K.; Jin, M.; Hwang, S. H.; Park, G. O.; Boo, J. H.; Han, T. H.; Kim, J. M. *Chem. Lett.* **2010**, *39*, 493.
- (5) Mooi, J.; Selwood, P. W. *J. Am. Chem. Soc.* **1952**, *74*, 1750.
- (6) Yamaguchi, K.; Yoshida, C.; Uchida, S.; Mizuno, N. *J. Am. Chem. Soc.* **2004**, *127*, 530.
- (7) Kitajima, N.; Fukuzumi, S.; Ono, Y. *J. Phys. Chem.* **1978**, *82*, 1505.
- (8) Zhao, Y.; Aoki, K. *Chem. Phys. Lett.* **2006**, *430*, 117.
- (9) Anders Nilsson, L. G. M. P.; Nørskov, J. K. *Chemical Bonding at Surfaces and Interfaces*; Elsevier: Amsterdam, 2008.
- (10) Erbil, H. Y. *Surface Chemistry Of Solid and Liquid Interfaces*, 1st ed.; Blackwell Publishing Ltd.: Oxford, 2006.
- (11) Wada, Y.; Uchida, S.; Nakamura, M.; Akamine, K. *J. Nucl. Sci. Technol.* **1999**, *36*, 169.
- (12) Tipping, P. *Int. J. Pressure Vessels Piping* **1996**, *66*, 17.
- (13) Ekeröth, E.; Roth, O.; Jonsson, M. *J. Nucl. Mater.* **2006**, *355*, 38.
- (14) Jonsson, M. In *Recent Trends in Radiation Chemistry*; Wishart, J. F., Rao, B. S. M., Ed.; World Scientific: Singapore, 2010; p 301.
- (15) Haber, F.; Weiss, J. *Naturwissenschaften* **1932**, *20*, 948.
- (16) Spear, E. B. *J. Am. Chem. Soc.* **1908**, *30*, 195.
- (17) Satterfield, C.; Stein, T. *Ind. Eng. Chem.* **1957**, *49*, 1173.
- (18) Trummer, M.; Dahlgren, B.; Jonsson, M. *J. Nucl. Mater.* **2010**, *407*, 195.
- (19) Suh, M.; Bagus, P. S.; Pak, S.; Rosynek, M. P.; Lunsford, J. H. *J. Phys. Chem. B* **2000**, *104*, 2736.
- (20) Anpo, M.; Che, M.; Fubini, B.; Garrone, E.; Giamello, E.; Paganini, M. *Top. Catal.* **1999**, *8*, 189.
- (21) Lousada, C. M.; Jonsson, M. *J. Phys. Chem. C* **2010**, *114*, 11202.
- (22) Amorelli, A.; Evans, J. C.; Rowlands, C. C. *J. Chem. Soc., Faraday Trans. 1: Phys. Chem. Condens. Phases* **1988**, *84*, 1723.
- (23) Giamello, E.; Calosso, L.; Fubini, B.; Geobaldo, F. *J. Phys. Chem.* **1993**, *97*, 5735.
- (24) *Progress React. Kinet. Mech.* **2005**, *30*, 145.
- (25) Hiroki, A.; LaVerne, J. A. *J. Phys. Chem. B* **2005**, *109*, 3364.
- (26) Becke, A. D. *Phys. Rev. A* **1988**, *38*, 3098.
- (27) Lee, C.; Yang, W.; Parr, R. G. *Phys. Rev. B* **1988**, *37*, 785.
- (28) Becke, A. D. *J. Chem. Phys.* **1993**, *98*, 5648.
- (29) Stephens, P. J.; Devlin, F. J.; Chabalowski, C. F.; Frisch, M. J. *J. Phys. Chem.* **1994**, *98*, 11623.
- (30) Zhao, Y.; Truhlar, D. *Theor. Chem. Acc.: Theory, Comput., Model. (Theor. Chim. Acta)* **2008**, *120*, 215.
- (31) Henderson, M. A. *Surf. Sci. Rep.* **2002**, *46*, 1.
- (32) Ahdjoudj, J.; Minot, C. *Surf. Sci.* **1998**, *402–404*, 104.
- (33) Gong, X.-Q.; Selloni, A.; Batzill, M.; Diebold, U. *Nat. Mater.* **2006**, *5*, 665.
- (34) Brookes, I. M.; Muryn, C. A.; Thornton, G. *Phys. Rev. Lett.* **2001**, *87*, 266103.
- (35) Lousada, C. M.; Johansson, A. J.; Brinck, T.; Jonsson, M., to be published.
- (36) Choppin, G.; J.-O. L., Rydberg, J. *Radiochemistry and nuclear chemistry*, 2nd ed.; Butterworth-Heinemann Ltd: Oxford, 1995; Vol. 46.
- (37) Bailey, J. E. *Proc. R. Soc. London Ser. A, Math. Phys. Sci.* **1964**, *279*, 395.
- (38) Howard, C. J.; Sabine, T. M.; Dickson, F. *Acta Crystallogr., Sect. B* **1991**, *47*, 462.
- (39) Hanic, F.; Hartmanova, M.; Knab, G. G.; Urusovskaya, A. A.; Bagdasarov, K. S. *Acta Crystallogr., Sect. B* **1984**, *40*, 76.
- (40) Hochanadel, C. J. *J. Phys. Chem.* **1952**, *56*, 587.
- (41) Ghormley, J. A.; Stewart, A. C. *J. Am. Chem. Soc.* **1956**, *78*, 2934.
- (42) Deák, P. *Physica Status Solidi B* **2000**, *217*, 9.
- (43) *Jaguar*, version 7.7; Schrödinger, LLC: New York, 2011.
- (44) Staroverov, V. N.; Scuseria, G. E.; Tao, J.; Perdew, J. P. *J. Chem. Phys.* **2003**, *119*, 12129.
- (45) Santen, R. A. v.; Neurock, M.; Shetty, S. G. *Chem. Rev.* **2009**, *110*, 2005.
- (46) Chirita, P. *Chem. Biochem. Eng. Q.* **2009**, *23*, 259.
- (47) M. Murphy, D.; W. Griffiths, E.; C. Rowlands, C.; E. Hancock, F.; Giamello, E. *Chem. Commun.* **1997**, 2177.
- (48) Croiset; E.; Rice, F. S.; Hanush, G., R. *Hydrogen peroxide decomposition in supercritical water*; Wiley-Blackwell: Hoboken, NJ, ETATS-UNIS, 1997; Vol. 43.
- (49) *Radiation chemistry: From basics to applications in material and life sciences*; Belloni J., T. D., Mostafavi, M., Spothem-Maurizot, M., Eds.; EDP Sciences: Les Ulis Cedex, 2008.
- (50) Buxton, G. V.; Greenstock, C. L.; Helman, W. P.; Ross, A. B. *J. Phys. Chem. Ref. Data* **1988**, *17*, 513.
- (51) A. van Santen, R.; Neurock, M. *Molecular Heterogeneous Catalysis: A Conceptual and Computational Approach*; WILEY-VCH Verlag GmbH & Co. KGaA: Weinheim, 2006.
- (52) Jung, J.; Shin, H.-J.; Kim, Y.; Kawai, M. *J. Am. Chem. Soc.* **2011**, *133*, 6142.
- (53) Gong, X.-Q.; Selloni, A. *J. Catal.* **2007**, *249*, 134.
- (54) Liu, Z.-P.; Hu, P. *J. Am. Chem. Soc.* **2003**, *125*, 1958.
- (55) Bailey, C. L.; Mukhopadhyay, S.; Wander, A.; Searle, B. G.; Carr, J. M.; Harrison, N. M. *Phys. Chem. Chem. Phys.* **2010**, *12*, 6124.
- (56) Zhao, Y.; Truhlar, D. G. *Theor. Chem. Acc.* **2008**, *120*, 215.

- (57) Riley, K. E.; Hobza, P. *Wiley Interdiscip. Rev.: Comput. Mol. Sci.* **2011**, *1*, 3.
- (58) Johansson, A. J.; Zuidema, E.; Bolm, C. *Chem.—Eur. J.* **2010**, *16*, 13487.
- (59) Weibel, M. A.; Backstrand, K. M.; Curtiss, T. J. *Surf. Sci.* **2000**, *444*, 66.
- (60) Radha, A. V.; Bomati-Miguel, O.; Ushakov, S. V.; Navrotsky, A.; Tartaj, P. *J. Am. Ceram. Soc.* **2009**, *92*, 133.
- (61) Raz, S.; Sasaki, K.; Maier, J.; Riess, I. *Solid State Ionics* **2001**, *143*, 181.
- (62) Iskandarova, I. M.; Knizhnik, A. A.; Rykova, E. A.; Bagatur'yants, A. A.; Potapkin, B. V.; Korkin, A. A. *Microelectron. Eng.* **2003**, *69*, 587.
- (63) Okamoto, Y. *Appl. Surf. Sci.* **2008**, *255*, 3434.
- (64) Haase, F.; Sauer, J. *J. Am. Chem. Soc.* **1998**, *120*, 13503.
- (65) Egashira, M.; Kawasumi, S.; Kagawa, S.; Seiyama, T. *Bull. Chem. Soc. Jpn.* **1978**, *51*, 3144.
- (66) Vittadini, A.; Selloni, A.; Rotzinger, F. P.; Gr; auml; tzel, M. *Phys. Rev. Lett.* **1998**, *81*, 2954.
- (67) Hussain, A.; Gracia, J.; Nieuwenhuys, B. E.; Niemantsverdriet, J. *W. ChemPhysChem* **2010**, *11*, 2375.
- (68) Hammer, B.; Wendt, S.; Besenbacher, F. *Top. Catal.* **2010**, *53*, 423.
- (69) Huang, W. F.; Raghunath, P.; Lin, M. C. *J. Comput. Chem.* **2011**, *32*, 1065.
- (70) Zhang, P.; Navrotsky, A.; Guo, B.; Kennedy, I.; Clark, A. N.; Leshner, C.; Liu, Q. Y. *J. Phys. Chem. C* **2008**, *112*, 932.
- (71) Gorelov, B. M.; Morozovskaya, D. V.; Pashkov, V. M.; Sidorchuk, V. A. *Tech. Phys.* **2000**, *45*, 1147.